Article

Hierarchical Porous Bimetallic FeMn Metal−Organic Framework Gel for Efficient Activation of Peracetic Acid in Antibiotic Degradation

Lu Zheng, Jiarui Fu, Baolv Hua, Yi-nan Wu, Yifan Gu, Nianqiao Qin, and Fengting Li*

Cite This: *ACS Environ. Au* 2024, 4, 56−68

Read Online

| ACCESS | | Metrics & More | | Article Recommendations | | Supporting Information |

ABSTRACT: Effective techniques for eliminating antibiotics from water environments are in high demand. The peracetic acid (PAA)-based advanced oxidation process has recently drawn increasing attention for its effective antibiotic degrading capability. However, current applications of PAA-based techniques are limited and tend to have unsatisfactory performance. An additional catalyst for PAA activation could provide a promising solution to improve the performance of PAA. Bulky metal−organic framework gels (MOGs) stand out as ideal catalysts for PAA activation owing to their multiple advantages, including large surface areas, high porosity, and hierarchical pore systems. Herein, a bimetallic hierarchical porous structure, i.e., FeMn13BTC, was synthesized through a facile one-pot synthesis method and employed for PAA activation in ofloxacin (OFX) degradation. The optimized FeMn MOG/PAA system exhibited efficient catalytic performance, characterized by 81.85% OFX degradation achieved within 1 h owing to the specific hierarchical structure and synergistic effect between Fe and Mn ions, which greatly exceeded the performance of the only PAA-catalyzed system. Furthermore, the FeMn MOG/PAA system maintained >80% OFX degradation in natural water. Quenching experiments, electron spin resonance spectra, and model molecular degradation revealed that the primary reactive oxygen species responsible for the catalytic effect was R−O$^\bullet$, especially $CH_3C(=O)OO^\bullet$, with minor contributions of $^\bullet OH$ and $^1O_2$. Overall, introduction of the MOG catalyst strategy for PAA activation achieved high antibiotic degradation performance, establishing a paradigm for the design of heterogeneous hierarchical systems to broaden the scope of catalyzed water treatment applications.

KEYWORDS: *metal−organic framework gel, hierarchical porous structures, peracetic acid, advanced oxidation process, antibiotics*
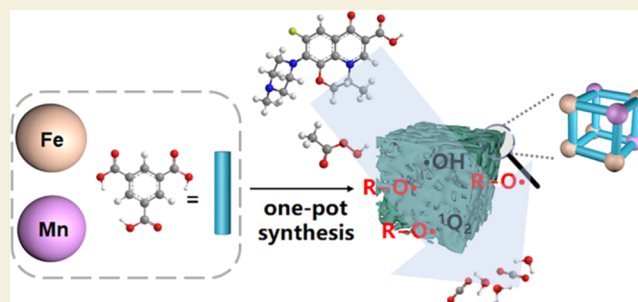
1. INTRODUCTION

Ofloxacin (OFX), a typical synthetic broad-spectrum quinolone antibiotic, has been widely used in the treatment of human diseases such as skin, respiratory, and urinary infections.[1] However, OFX exhibits low biodegradability, can linger in nature for a very long time, and is frequently detected in soil and water.[2] OFX concentrations of >1000 ng/L have been measured in the influents and effluents of sewage treatment plants, although its concentrations in surface water are generally lower by more than an order of magnitude.[3] Persistent OFX in the environment could impede microorganism growth and development and elevate the risk of antibiotic resistance developing in the biosphere, posing a threat to ecosystems and ultimately endangering humanity.[4] Given its limited biodegradability and associated risks, developing efficient degradation techniques for the OFX is imperative.

Among current treatment options for OFX degradation, such as adsorption and biodegradation, advanced oxidation processes (AOPs) are powerful techniques, in which pollutants are decomposed through the production of strong oxidants, thereby avoiding secondary pollution.[5] Peracetic acid (PAA)-based advanced oxidation has become an emerging AOP technique for water treatment in recent years. PAA demonstrates a similar oxidation potential as H_2O_2, with values of 1.76 and 1.77 V, respectively.[6] Nevertheless, PAA has a much lower O−O bond energy (159 kJ mol^{-1}) than that of H_2O_2 (213 kJ mol^{-1}), indicating that PAA can be more easily activated.[7] Additionally, the disinfecting capability of PAA makes it particularly attractive in water treatment.[8] To date, PAA-based advanced oxidation has displayed excellent degradation capacity for dyes, endocrine disrupters, antibiotics, etc.,[9] although its application in antibiotic degradation has mainly focused on β-lactam and sulfonamide antibiotics.[9,10] In order to expand the application range and improve the catalytic performance of PAA-based techniques, researchers have developed new systems, such as the use of UV/PAA for
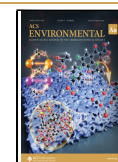
fluoroquinolone degradation. Nonetheless, further investigation is warranted for the use of PAA-based advanced oxidation for OFX degradation.[11,12]

Apart from external energy sources such as ultraviolet irradiation, ultrasonic irradiation, and heat, utilization of an additional catalyst for PAA activation proves to be an ideal solution. Co-, Fe-, and Mn-based materials have demonstrated efficient PAA activation in AOPs.[8] The FeMn bimetallic system has been widely recognized as a highly efficient catalyst with superior performance compared to monometallic materials owing to its dual reaction site construction and electron transfer acceleration, and the excellent catalytic properties of such bimetallic materials have been proven in Fenton-like reactions and persulfate-based AOPs.[13,14] Notably, application of the FeMn bimetallic system in PAA-based AOPs has not been previously reported. For these reasons, we hypothesized that PAA activation by such a bimetallic system would be key to enhancing the performance of the PAA-based advanced oxidation technology.

Apart from the choice of catalytic elements, the selection of the specific additional catalyst also requires careful consideration. Metal−organic frameworks (MOFs), composed of organic ligands and metal nodes, stand out as candidate catalysts in AOPs with a number of advantages, including their large specific surface areas, high porosity, tunable constitution, and abundant active sites.[15,16] Recently, Liu et al. first reported the use of a cobalt MOF (ZIF-67) as a catalyst to activate PAA for sulfachloropyridazine degradation, shedding light upon the potential applicability of MOFs in PAA-based AOPs.[17] Nonetheless, MOFs have certain limitations in actual practice. For example, the micropore-dominated pore structure of MOFs restricts mass transfer during catalysis, thereby suppressing degradation performance, while powder-phase MOFs are potentially problematic, as they can easily disperse in the environment and are difficult to recycle. Very recently, metal−organic framework gels (MOGs) have gained increasing attention, leading to hierarchical porous structures without templates or post-treatment and macroscopic monoliths. The introduction of MOGs is considered a potential breakthrough for industrial applications of MOF materials.[18]

However, maintaining the hierarchical porous structure of MOG materials requires an activation method, such as supercritical CO_2 and freeze drying, because intense capillary forces generated during common thermal activation can lead to macropore and mesopore collapse. These rigorous activation conditions limit the production and application of such materials. Recently, Fu et al. reported a method to control the crystalline state of MOGs by adjusting the reactant concentration, reaction time, and reaction temperature, which preserved the hierarchical porous structure of MOGs through common drying activation.[19] Meanwhile, modulating the MOF structure via defect engineering, such as the employment of heterogeneous metal ions, is recognized as an efficient strategy to generate hierarchical porous structures and improve catalytic performance.[20]

Herein, an FeMn bimetallic MOG with a hierarchical porous structure (FeMn13BTC) was carefully prepared and used as a catalyst to activate PAA for OFX degradation. The monolithic hierarchical MOG, obtained through one-pot synthesis followed by common drying, was produced by deliberately adjusting the metal salt ratio and synthetic temperature rather than using traditional supercritical CO_2 or freeze drying. The simple synthetic strategy contributes to optimal application of

MOGs and their scaled-up production. Additionally, the chemical composition, crystallinity, specific surface area, pore diameter distribution, and morphology of the catalyst were characterized. Subsequently, OFX degradation performance based on the MOG/PAA system was investigated, taking into account factors such as the choice of the catalyst, PAA concentration, pH, catalyst dosage, coexisting substances, and OFX concentration. Due to the hierarchical porous structure and synergistic effect between Fe and Mn, the optimized catalyst exhibited enhanced degradation performance compared to other catalysts, achieving >80% degradation in natural water. Analysis of the degradation mechanism indicated that OFX was disintegrated through three possible pathways, with attack mainly from $R-O^{\bullet}$, especially $CH_3C(=O)OO^{\bullet}$. The efficient catalytic performance of synthetic MOGs for PAA-based AOPs increases their applicability in water treatment and supports the effectiveness of the FeMn bimetallic system for PAA-based AOPs as well as PAA-based AOPs for OFX degradation.

2. MATERIALS AND METHODS

2.1. Materials

All solvents and reagents used in this study were commercially attained. Ferric nitrate nonahydrate ($Fe(NO_3)_3 \cdot 9H_2O$, 98%), manganese dinitrate hexahydrate ($Mn(NO_3)_2 \cdot 6H_2O$, 98%), and 2,4-hexadiene (>95%) were supplied by TCI Shanghai Co., Ltd. (Shanghai, China). Hydrogen peroxide (H_2O_2, 30%), *N,N*-dimethylformamide (DMF), and *tert*-butyl alcohol (TBA) were analytic grade and provided by Sinopharm Chemical Reagent Co., Ltd. (Shanghai, China). Trimesic acid (H_3BTC, 97%) and ofloxacin (OFX, 98%) were purchased from Shanghai Wokai Pharmaceutical Co., Ltd. (Shanghai, China). Carbamazepine (CBZ, 99%) was provided by Shanghai Macklin Biochemical Co., Ltd. (Shanghai, China). Peracetic acid (PAA) was supplied by Haianfushen Pharmaceutical Co., Ltd. (Nantong, China). 5,5-Dimethyl-1-pyrroline N-oxide (DMPO) and 4-amino-2,2,6,6-tetramethylpiperidine (TEMP) were provided by Aladdin Bio-Chem Technology Co., Ltd. (Shanghai, China). Deionized water was produced via an ultrapure water system (Master touch-S15; Hitech, Beijing, China).

2.2. Characterizations

Powder X-ray diffraction patterns were collected via a Rigaku Ultima IV X-ray powder diffractometer equipped with Cu Kα radiation (λ = 1.5418 Å) and a scanning rate of 2°/min. Fourier-transform infrared spectra (FTIR) were recorded via a Thermo Scientific Nicolet iS5. Scanning electron microscopy (SEM; Regulus8100) and transmission electron microscopy (TEM; Tecnai G2 20) were used for microstructure observation. N_2 adsorption−desorption measurements were conducted with a Belsorp-Max instrument. The materials underwent pretreatment by heating at 120 °C under vacuum for 12 h before testing. The specific surface areas and pore sizes were calculated based on Brunauer−Emmett−Teller (BET) and Barret−Joyner−Halenda (BJH) theories, respectively. The concentrations of OFX and carbamazepine were identified via an Agilent 1220 liquid chromatograph equipped with a Waters BEH C18 column. X-ray photoelectron spectroscopy (XPS; Thermo Scientific K-Alpha with Al Kα radiation) was used to characterize the chemical states of the materials. The catalyst used for XPS characterization was obtained after FeMn13BTC was employed for 1 h as a catalyst (OFX 5 mg/L, PAA 1.034 mM, catalyst 10 mg/L, pH 7). Electron spin resonance (ESR) spectra were obtained with a Bruker EMXplus-6/1 instrument.

2.3. Preparation of the FeBTC MOG

The FeBTC MOG was synthesized following a procedure similar to that described by Lohe et al., with a small modification.[21] First, $Fe(NO_3)_3 \cdot 9H_2O$ (15 mmol) was dissolved in 20 mL of ethanol, while H_3BTC (10 mmol) was dissolved in another 20 mL of ethanol. Then,
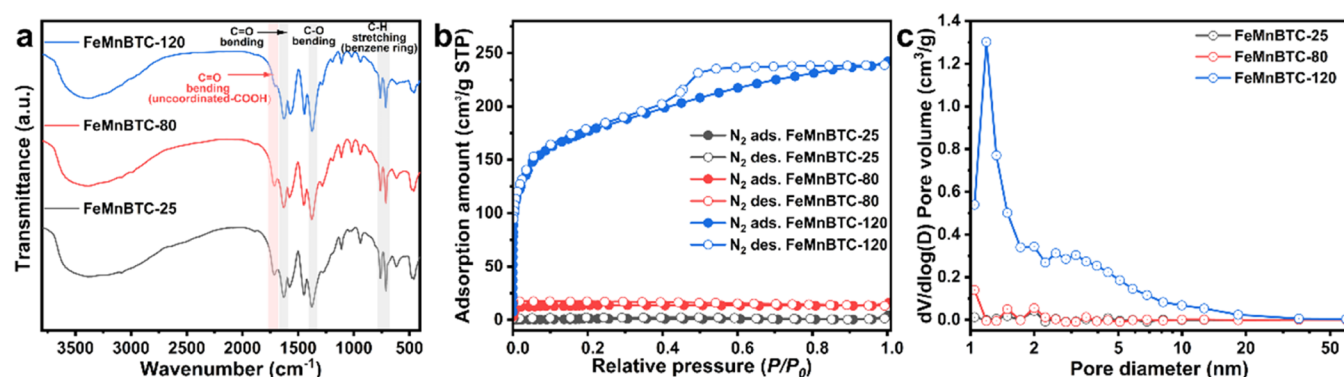
Figure 1. (a) FTIR spectra, (b) N$_2$ adsorption−desorption isotherms, and (c) pore diameter distributions (analyzed by BJH theory, x-axis in the logarithmic scale) of the FeMnBTC MOGs synthesized at different temperatures.

the two solutions were mixed and reacted for 24 h at 25 °C. After the reaction, the resulting product was washed three times with ethanol and dried in air.

2.4. Preparation of the Bimetallic FeMn MOG

The bimetallic FeMn MOG was synthesized by altering the synthetic temperature and metal salt ratio while keeping a fixed total amount of metal salts at 15 mmol. The metal salts, (Fe(NO$_3$)$_3$·9H$_2$O and Mn(NO$_3$)$_2$·6H$_2$O), and H$_3$BTC were separately dissolved in 20 mL of DMF. The solutions were then mixed together and heated at a specific temperature for 24 h. After the reaction, the product was washed three times with ethanol and dried in air to obtain the final, synthesized bimetallic FeMn MOG.

2.5. OFX Degradation Experiments by MOGs Activating PAA

The PAA solution was prepared by mixing solution A (containing acetic and sulfuric acids) and solution B (containing H$_2$O$_2$) in a ratio of 27:23 (V_A/V_B). The mixture was left for 24 h for reaction. The resulting PAA solution was used 24 h after production. To identify the PAA and H$_2$O$_2$ concentrations in the prepared PAA solution, a titration method was employed.[10] Initially, the total PAA and H$_2$O$_2$ concentrations were measured via indirect iodometric titration. Potassium iodide and ammonium molybdate were added to the prepared PAA solution, resulting in the production of iodine, which was titrated against sodium thiosulfate. Next, the H$_2$O$_2$ concentration in the prepared PAA solution was identified by using potassium permanganate as the titrant. Finally, the PAA concentration in the PAA solution was calculated by subtracting the H$_2$O$_2$ concentration from the combined PAA and H$_2$O$_2$ concentrations obtained from previous titrations.

Beaker experiments were carried out to examine OFX degradation by the MOG/PAA system at room temperature (approximately 25 °C). The procedure involved the addition of a catalyst to a solution of OFX, with a total volume of 100 mL. Sodium hydroxide (NaOH) and hydrochloric acid (HCl) were used to adjust the pH of the solutions. A certain amount of PAA was then added to the suspension with magnetic stirring at 400 r/min. At certain time intervals during the reaction, aliquots of solution were withdrawn using an injection syringe and were subsequently passed through a 0.22 μm filter. To quench the reaction, 10 μL of 100 mM Na$_2$S$_2$O$_3$ was added to the filtered samples. The OFX concentration in the samples was identified by liquid chromatography. For OFX detection, mobile phase A was 0.1% formic acid, while mobile phase B was acetonitrile (ACN). The mobile phase was an 80:20 mixture (V_A/V_B) and the detector wavelength was set at 275 nm. For carbamazepine detection, the mobile phase ratio was changed to 40:60 and the detector wavelength was shifted to 285 nm.

The intermediates of OFX degradation were identified via high-performance liquid chromatography quadrupole time-of-flight mass spectrometry (HPLC-QToF-MS; Agilent 1290 UPLC, Agilent 6550 Q-TOF). The mobile phase consisted of 0.1% aqueous formic acid

(phase A) and ACN (phase B) at a flow rate of 0.3 mL/min. The column was eluted with 5% ACN for 2.0 min, followed by a gradual increase in the ACN ratio to 80% at 10.0 min, which was held for 6.0 min. Finally, the ACN ratio was decreased back to 5% in 2.0 min, which was held for 2.0 min. Mass spectrometry was operated in positive ion mode with a voltage of 4000 V.

3. RESULTS AND DISCUSSION

3.1. Characterization

The bimetallic FeMn MOG was fabricated at 1:1 metal salt ratio and reacted at 25, 80, and 120 °C, resulting in materials named FeMnBTC-25, FeMnBTC-80, and FeMnBTC-120, respectively. The XRD spectra of these materials exhibited a similar pattern as that of the monometallic MOG FeBTC. This similarity suggested that incomplete coordination between organic ligands and metal ions (Fe, Mn) might have influenced the crystallinity of the bimetallic MOG[22] (Figure S1). The FTIR spectra of the fabricated materials presented in Figure 1a show information about the functional groups present. As shown in Figure 1a, characteristic peaks for all materials were observed at 711, 760, 1380, and 1630 cm^{-1}. The peaks at 711 and 760 cm^{-1} were attributed to the C−H stretching on the benzene ring. The peak at 1380 cm^{-1} corresponded to the bending vibration of C−O bonds, while that at 1630 cm^{-1} was attributed to bending of the C=O bond.[23] Interestingly, as the synthetic temperature was increased to 120 °C, the intensity of the characteristic peak at approximately 1710 cm^{-1} was significantly reduced, which was attributed to the C=O bending of uncoordinated H$_3$BTC. This finding suggested that there was less unreacted H$_3$BTC and a higher degree of coordination between metal ions and H$_3$BTC ligands at higher temperatures, indicating more complete incorporation of the ligand into the bimetallic MOG at higher temperatures.[20] The specific surface areas and pore structures of the fabricated materials were characterized using N$_2$ adsorption−desorption measurements[22] (Figure 1b,c). FeMnBTC-25 exhibited extremely low N$_2$ adsorption, indicating the absence of accessible micropores in the structure. FeMnBTC-80 showed increased N$_2$ adsorption, at 15.92 cm^3/g. The fully coincident adsorption and desorption curves indicated the sole presence of micropores in the material. As the synthetic temperature was further increased, FeMnBTC-120 displayed a significantly higher N$_2$ adsorption, especially in the low-pressure region. Moreover, the appearance of a hysteresis loop in the adsorption−desorption curves suggested the coexistence of micropores and mesopores in the material. In the case of the monometallic FeBTC MOG, Fe ions were capable of

coordinating with H_3BTC at room temperature (approximately 25 °C), leading to the formation of a gel structure.[21] However, the introduction of Mn ions into the bimetallic FeMn MOG disrupted the original crystal nucleus growth, preventing network structure formation at room temperature. Consequently, the resulting bimetallic MOG did not possess micropores. As the synthetic temperature was increased, Mn ions gradually participated in the coordination process, giving rise to a continued crystal nucleus growth. Eventually, a gel structure with a network arrangement was formed in the bimetallic MOG. In accordance with the findings presented in Table 1, the specific surface areas and pore volumes (especially

Table 1. Comparison of Surface Areas, Total Pore Volumes, and Mesopore Volumes between MOGs Synthesized at Different Temperatures

materials	S_{BET} (m^2/g)	V_{total} (cm^3/g)	$V_{mesopore}$ (cm^3/g)
FeMnBTC-25	2.99		9.2964×10^{-4}
FeMnBTC-80	47.14	0.0233	2.3648×10^{-3}
FeMnBTC-120	621.88	0.3728	0.1679

mesopore volumes) of the synthesized products gradually increased along with increased synthesis temperature.[22] These results indicated that the optimal synthetic temperature for achieving a hierarchically porous structure in the FeMn bimetallic MOG was 120 °C.

By adjusting the metal salt ratio, the properties of the synthetic FeMn bimetallic MOGs were further controlled. Three different compositions, i.e., FeMn31BTC, FeMn11BTC, and FeMn13BTC, were synthesized at 120 °C with molar ratios of $Fe(NO_3)_3 \cdot 9H_2O/Mn(NO_3)_2 \cdot 6H_2O$ at 3:1, 1:1, and

1:3, respectively. By contrast, FeBTC was synthesized at room temperature (approximately 25 °C). Although all of the materials exhibited similar broad peaks as FeBTC, the XRD pattern of FeMn31BTC displayed multiple small sharp peaks within the range of 30−55° (Figure.S2). The presence of these small sharp peaks was attributed to two factors. First, because the proportion of Fe ions was relatively high in FeMn31BTC (molar ratio of $Fe(NO_3)_3 \cdot 9H_2O/Mn(NO_3)_2 \cdot 6H_2O = 3:1$), the inhibition of crystal nucleus growth by Mn ions was negligible. Second, the increased temperature further enhanced the crystallinity of Fe ions coordinated with ligands compared with FeBTC, which was synthesized at room temperature. The combination of a higher Fe proportion and an elevated temperature contributed to the formation of small sharp peaks in the XRD pattern of FeMn31BTC. FTIR spectral analysis revealed that the synthesized materials retained characteristic peaks of FeBTC, such as C−H stretching on the benzene ring (711 and 760 cm^{-1}), C−O bending vibration (1380 cm^{-1}), and C=O bending vibration (at approximately 1630 cm^{-1}), as previously mentioned (Figure 2a). Furthermore, with an increasing proportion of Mn ions in the bimetallic MOG, the peak corresponding to the C=O bending vibration exhibited a gradual red shift toward 1619 cm^{-1} (Figure 2b). This shift indicated that Mn ions progressively coordinated into the MOG structure.[24] As a result, the Fe and Mn ions coordinated with H_3BTC, forming a bimetallic organic framework gel. The coordination of Fe and Mn ions in the bimetallic MOG resulted in significant changes in the specific surface area and pore structure. Although the specific surface area decreased as the proportion of Mn ions increased, the presence of hysteresis loops in the N_2 adsorption−desorption curves indicated that mesopores were present in the material (Figure 2c). When the
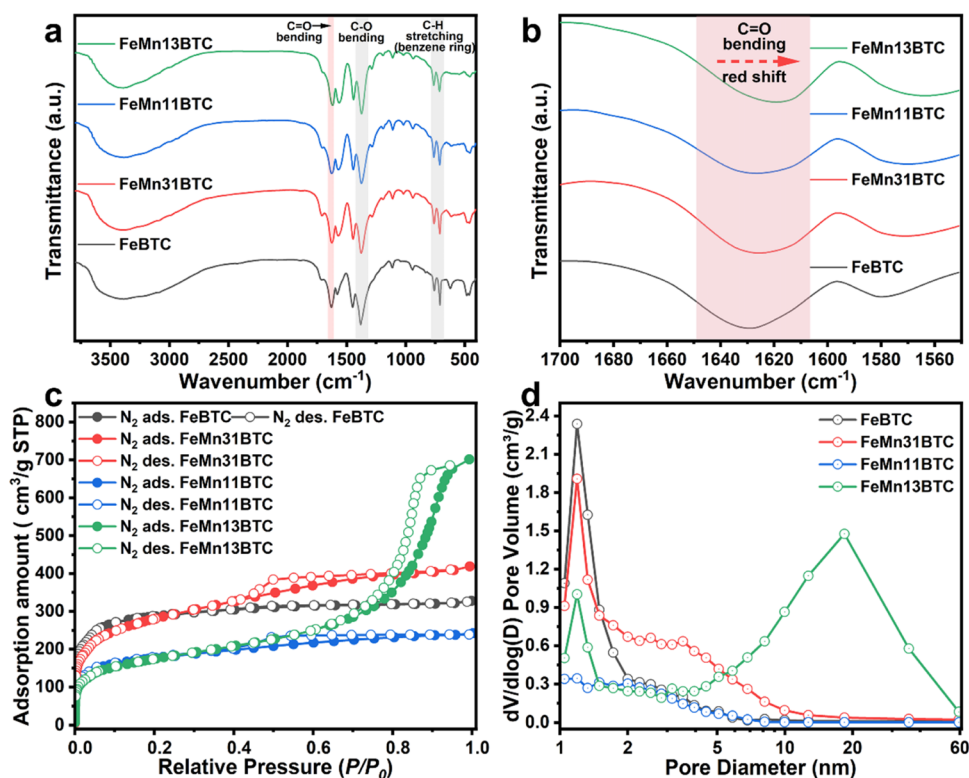

Figure 2. (a) FTIR spectra, (b) detailed C=O bending in FTIR spectra, (c) N_2 adsorption−desorption isotherms, and (d) pore diameter distributions (analyzed by BJH theory, x-axis on the logarithmic scale) of MOGs synthesized with different metal salt ratios.

molar ratio of $Fe(NO_3)_3 \cdot 9H_2O/Mn(NO_3)_2 \cdot 6H_2O$ was higher than 1:3, the pore diameter distribution was mostly limited to within 10 nm (Figure 2d). However, the upper limit of the pore diameter extended to 60 nm when the ratio declined to 1:3, while the pore volume and average pore diameter increased to 1.0953 cm^3/g and 5.27 nm, respectively, with a higher proportion of mesopores. These values were 2.17 and 3.54 times larger than those of FeBTC, respectively (Table 2).

Table 2. Comparison of Surface Areas, Pore Volumes, and Pore Diameters between MOGs Synthesized with Different Metal Salt Ratios

materials	S_{BET} (m^2/g)	V_{tqtal} (cm^3/g)	average pore diameter (nm)	$V_{micropore}/V_{mesopore}$
FeBTC	1027.10	0.5049	1.49	4.442
FeMn31BTC	982.62	0.6044	1.99	1.563
FeMn11BTC	621.88	0.3728	1.84	1.906
FeMn13BTC	615.70	1.0953	5.27	0.117

The morphologies of FeBTC and FeMn13BTC were characterized via SEM and TEM. FeBTC (Figure 3a) consisted of ball-like nanoparticles of <50 nm size. These nanoparticles exhibited a dense packing arrangement, and no significant porosity was observed. By contrast, FeMn13BTC (Figure 3b) comprises spherical nanoparticles with varying sizes, ranging from 30 to 100 nm. Moreover, a higher degree of porosity was evident for FeMn13BTC, with the formation of interspaces among the packed particles. TEM analysis provided further evidence of the network structure of FeMn13BTC, exhibiting abundant mesopores and a few macropores cross-linked by spherical aggregates (Figure 3c). High-resolution TEM was utilized to observe the microstructure of FeMn13BTC; however, no obvious lattice fringe was found (Figure S3). The results obtained from electronic microscopy and pore diameter distribution analysis indicated that FeMn13BTC had a hierarchical micro−meso−macroporous structure. The successful fabrication of a hierarchical porous bimetallic MOG was attributed to the introduction of heterogeneous metal ions.[25]

XPS analysis was conducted to examine the chemical environment and valence states of the elements in FeBTC and FeMn13BTC. The XPS spectra (Figure S4) displayed the characteristic peaks of C 1s, O 1s, and Fe 2p at approximately 286, 532, and 712 eV, respectively, in both FeBTC and FeMn13BTC. In FeMn13BTC, an additional peak at 640 eV indicated the presence of Mn ions. Further analysis of the C 1s spectrum revealed subpeaks corresponding to C−C, C−O, and C═O bonds (Figure 4a). The results suggested the existence of benzene rings and carboxyl groups derived from the coordinated ligands.[26] Deconvolution of the O 1s spectrum resulted in peaks at 531.8 and 533.5 eV, which were attributed to C−O and C═O bonding, respectively (Figure 4b). The Fe 2p orbital exhibited double peaks at approximately 712 and 725 eV, indicating the valence state of Fe as Fe(III) (Figure 4c).[27] However, the coordination of Mn ions changed the chemical environment of the Fe element, reflected as the Fe 2p orbital of FeMn13BTC having increasingly higher energy compared to that of FeBTC (Figure 4c). The Mn 2p orbital of FeMn13BTC displayed two characteristic peaks and one satellite peak (Figure 4d), with the peak at 641.5 eV indicating the presence of Mn(II), while the peak at 643.2 eV suggested the presence of Mn(IV). The high intensity of the satellite peak at 646.9 eV, corresponding to Mn(II), demonstrated the crucial role of Mn(II) in FeMn13BTC.[28]

3.2. Bimetallic MOGs as a Catalyst for PAA Oxidation

3.2.1. Catalytic Performance of Different MOGs.
FeBTC, FeMn31BTC, FeMn11BTC, and FeMn13BTC were used as catalysts to activate PAA for OFX degradation. The results in Figure 5a show that the FeBTC/PAA system achieved approximately 56.78% OFX degradation within 1 h. Moreover, OFX degradation was continuously enhanced as the proportion of Mn ions was increased in the synthesis system. Among the tested materials, the FeMn13BTC/PAA system displayed the highest OFX degradation with 78.41%, indicating a 38% increase in catalytic performance compared to the monometallic MOG FeBTC. The degradation data of the fast reaction stage (within 20 min) were fitted using kinetic models (Table S1), which indicated that the pseudo-second-order model was more suitable for describing the OFX degradation kinetics. The FeMn13BTC/PAA system exhibited the highest degradation efficiency with a rate constant of 0.03172 L mg^{-1} min^{-1}, while the other systems exhibited lower efficiencies with rate constants <0.021 L mg^{-1} min^{-1}. The above-mentioned results indicated that FeMn13BTC demonstrated the best catalytic performance for PAA activation in the OFX
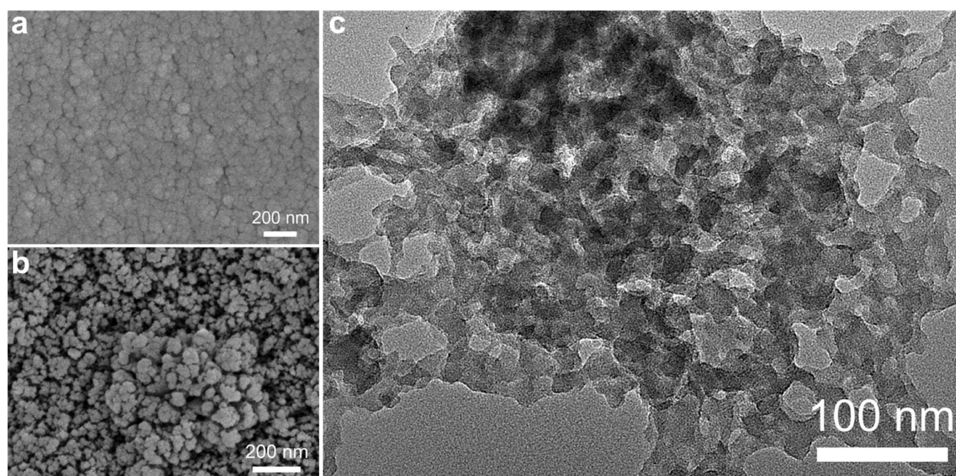

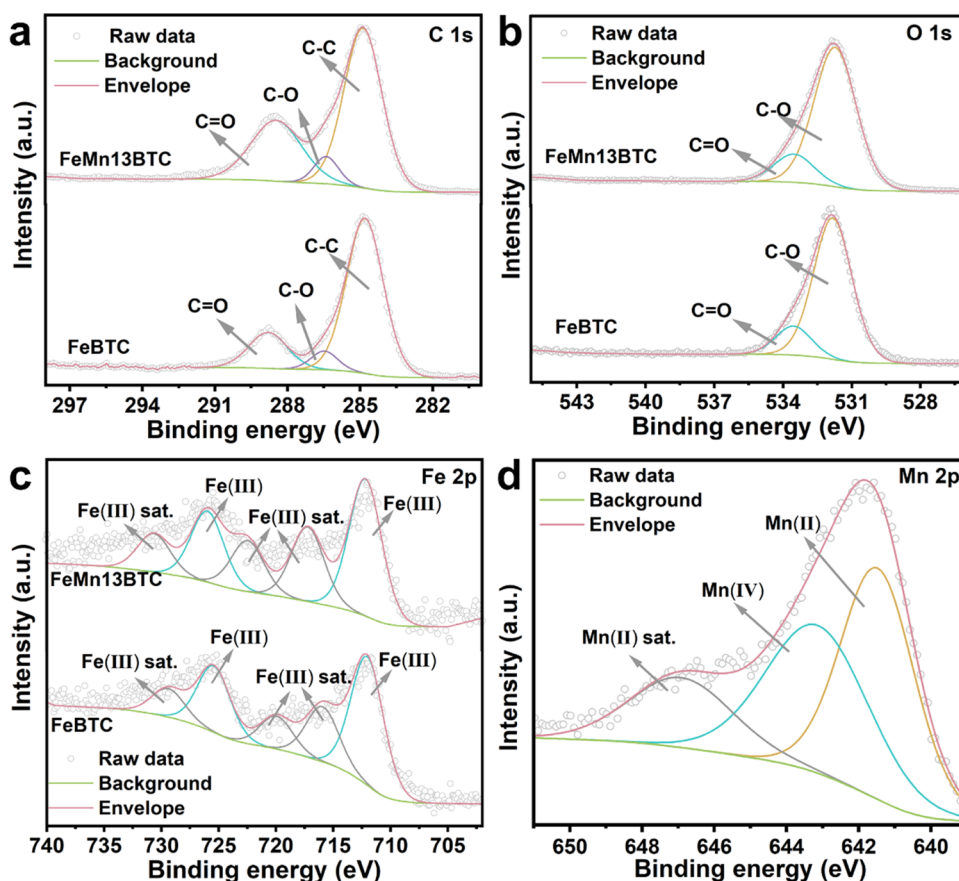**Figure 3.** SEM images of (a) FeBTC and (b) FeMn13BTC, and (c) TEM image of FeMn13BTC.

Figure 4. (a) C 1s spectra, (b) O 1s spectra, and (c) Fe 2p spectra of FeBTC and FeMn13BTC. (d) Mn 2p spectra of FeMn13BTC.
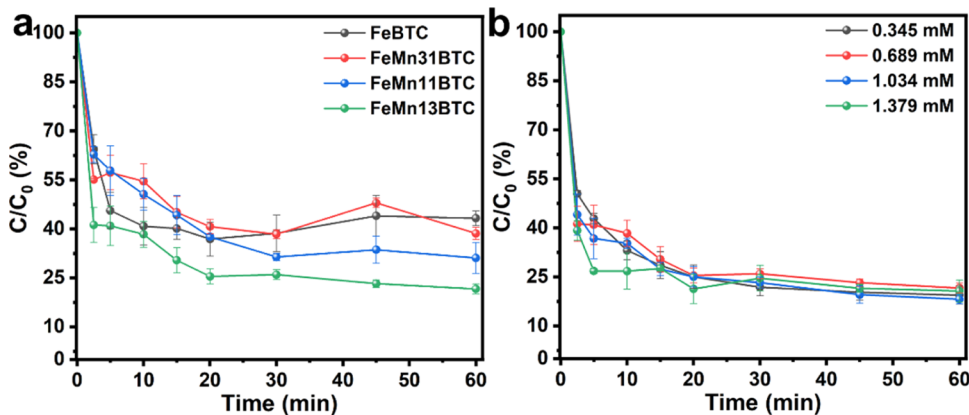

Figure 5. (a) Comparison of OFX degradation catalyzed by different MOGs, OFX 5 mg/L, pH 7, catalyst 0.1 g/L, and PAA 0.689 mM. (b) Impact of the PAA amount on OFX degradation based on the FeMn13BTC/PAA system, OFX 5 mg/L, pH 7, and catalyst 0.1 g/L.

degradation. The superior catalytic performance of FeMn13BTC was attributed to two main factors: pore structure and the Fe/Mn ratio. As previously discussed with regard to N_2 adsorption−desorption, although FeMn13BTC did not have the highest specific surface area, it exhibited a significantly larger average pore diameter, at least 2.6 times larger than that of the other materials tested. Additionally, FeMn13BTC displayed a wider pore diameter distribution. These characteristics of FeMn13BTC, including its abundant mesopores and macropores, contributed to mass transfer during the catalytic reaction, leading to a faster reaction rate compared to other synthesized materials.[29] Meanwhile, the proportion of Mn in the product increased as the metal salt

ratio ($Fe(NO_3)_3 \cdot 9H_2O/Mn(NO_3)_2 \cdot 6H_2O$) decreased. This adjustment strengthened the synergistic effect between Fe and Mn, ultimately leading to the enhanced catalytic performance of FeMn13BTC.[30]

3.2.2. Factors Influencing the Catalytic Performance of FeMn13BTC. As shown in Figure 5b, the influence of the PAA concentration on the catalytic performance of FeMn13BTC was not significantly pronounced. Within the range of 0.345−1.379 mM PAA, OFX degradation showed minor fluctuations between 78.41 and 81.85%. Notably, at an optimal PAA concentration of 1.034 mM, OFX degradation reached its highest value at 81.85%, accompanied by the highest kinetic constant of 0.03433 L mg^{-1} min^{-1} (Table S2).
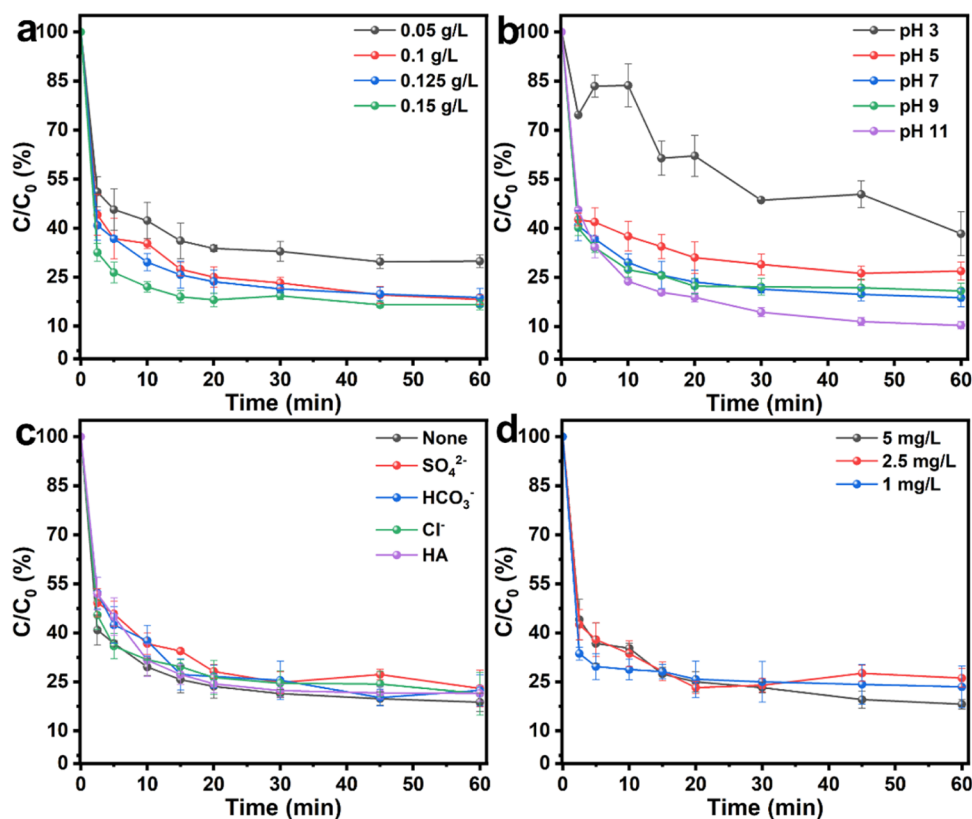
Figure 6. (a) Impact of the catalyst amount (OFX 5 mg/L, pH 7, PAA 1.034 mM), (b) pH (OFX 5 mg/L, catalyst 0.1 g/L, PAA 1.034 mM), (c) coexisting substances (anions 5 mg/L, HA 2 mg/L, OFX 5 mg/L, catalyst 0.1 g/L, PAA 1.034 mM), and (d) OFX concentration (pH 7, catalyst 0.1 g/L, PAA 1.034 mM) on OFX degradation based on the FeMn13BTC/PAA system.

Nevertheless, a slight decrease in OFX degradation was observed upon a further increase in PAA concentration, which may have been attributed to radical quenching resulting from excessive PAA.[8] However, the kinetic constant increased to 0.04182 L mg^{-1} min^{-1} under such conditions.

The impact of the catalyst dosage on the performance of the FeMn13BTC/PAA system was found to be twofold: a low catalyst dosage had a detrimental effect on degradation performance, while a high catalyst dosage primarily accelerated the reaction kinetics, as evidenced in Figure 6a and Table S3. When the catalyst dosage was decreased to 0.05 g/L, OFX degradation dropped to 70.15%. Nonetheless, within the dosage range of 0.1−0.15 g/L, OFX degradation did not differ significantly and remained >80%. At a dosage of 0.15 g/L, the kinetic constant increased by 61% compared to a dosage of 0.1 g/L (0.03433 L mg^{-1} min^{-1}), reaching 0.05540 L mg^{-1} min^{-1}.

The pH influence experiments revealed that the FeMn13BTC/PAA system was hindered by the presence of H$^+$ ions, indicating that OFX degradation was more effective in an alkaline environment. Figure 6b illustrates the decrease in OFX degradation based on the FeMn13BTC/PAA system as the solution became more acidic, with values of 61.68% at pH 3 and 73.07% at pH 5. At pH 9, the total OFX degradation remained similar to that at pH 7, but the kinetic constant increased by 18%, reaching 0.04054 L mg^{-1} min^{-1}. A more significant improvement was observed at pH 11, achieving nearly 90% OFX degradation and a kinetic constant of 0.04995 L mg^{-1} min^{-1} (Table S4). OFX exists as a cation at pH < 5.97 and an anion at pH > 9.28 and is neutral at pH values between 5.97 and 9.28.[31] The dissociation constant of PAA is approximately 8.2 and PAA$^-$ becomes the predominant species

when the pH exceeds this value.[32] As shown in Figure S5, the isoelectric point of FeMn13BTC was at pH 2.81, and its surface was negatively charged above this pH. However, OFX degradation under alkaline conditions was not suppressed by electrostatic repulsion between FeMn13BTC, PAA$^-$, and OFX. The increased OFX degradation may be attributed to increased PAA hydrolysis with rising pH, resulting in more efficient PAA activation based on the FeMn13BTC/PAA system in an alkaline environment.[32] In addition to less PAA hydrolysis, deteriorating OFX degradation may be caused by the dissolution of metal ions under acidic conditions. Thus, although electrostatic attraction may promote the OFX adsorption on the surface of FeMn13BTC, collapse of the catalyst structure caused by metal ion dissolution is destructive to the OFX degradation performance.[33]

The presence of various inorganic anions and organic substances in natural water can potentially affect the degradation performance of FeMn13BTC/PAA. Therefore, OFX degradation based on the FeMn13BTC/PAA system was investigated in the presence of Cl$^-$, SO$_4^{2-}$, HCO$_3^-$, and humic acid (HA). As shown in Figure 6c, these coexisting substances had minimal effects on the degradation performance of FeMn13BTC/PAA. OFX degradation remained >77%, and the kinetic constants displayed only slight fluctuations within the range of 0.02785−0.03495 L mg^{-1} min^{-1} (Table S5). Among them, SO$_4^{2-}$ had the greatest impact on OFX degradation and kinetics, decreasing to 77.03% and 0.02785 L mg^{-1} min^{-1}, respectively. To evaluate the practical potential of FeMn13BTC/PAA in natural water, water samples were collected from the Dianshan Lake and artificially spiked with 5 mg/L OFX. The results indicated that the FeMn13BTC/PAA
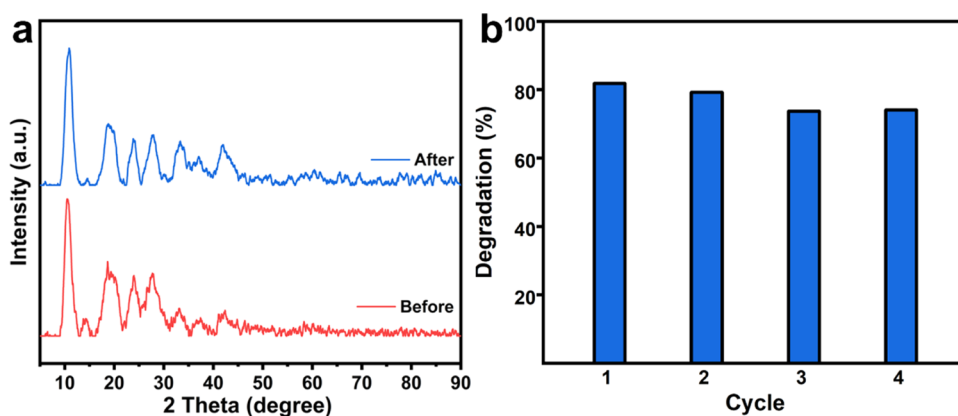
Figure 7. (a) XRD patterns of FeMn13BTC before and after catalysis. (b) Cycle experiments of FeMn13BTC/PAA for OFX degradation. OFX 5 mg/L, catalyst 0.1 g/L, PAA 1.034 mM, and pH 7.
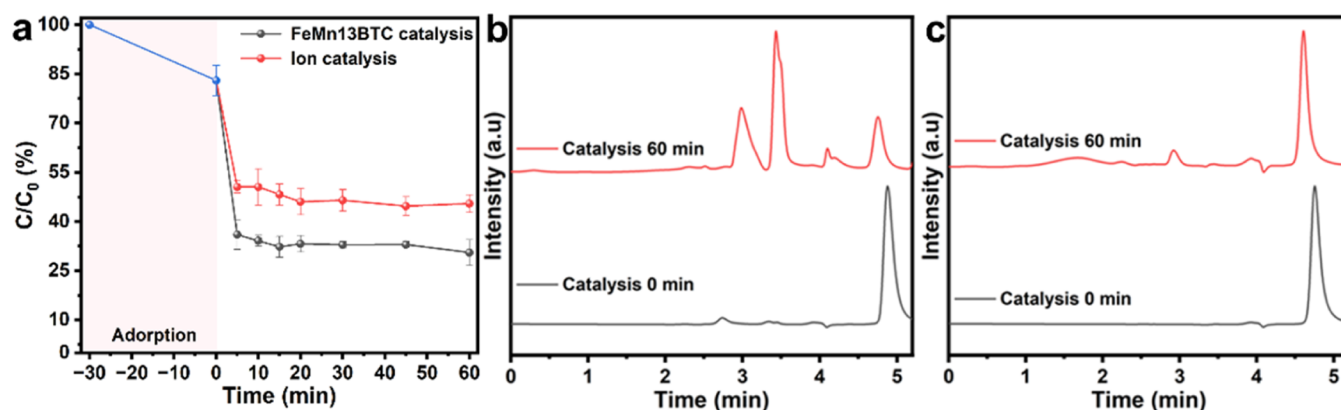

Figure 8. (a) OFX removal after 30 min of preadsorption with FeMn13BTC without (gray line) and with (red line) filtration before PAA was added to the system, OFX 5 mg/L, catalyst 0.05 g/L, PAA 1.034 mM, and pH 7. Chromatographic peaks before and after OFX degradation catalyzed by (b) FeMn13BTC/PAA system and (c) FeMn13BTC/H_2O_2 system.

system was able to degrade >80% OFX. Additionally, the catalytic performance of the FeMn13BTC/PAA system at low OFX concentrations was investigated by reducing the initial OFX concentration to 1 mg/L. As presented in Figure 6d, the FeMn13BTC/PAA system exhibited satisfactory degradation at both high and low OFX concentrations, with >73% degradation. These findings preliminarily suggested that the FeMn13BTC/PAA system is promising for practical applications in water treatment scenarios. A comparison of the FeMn13BTC/PAA system with other PAA-based AOP techniques is presented in Table S6.

The stability of FeMn13BTC was tested in cycle experiments and assessed via XRD and ICP. The XRD patterns were almost consistent before and after catalysis, demonstrating the firm structure of FeMn13BTC during catalysis (Figure 7a). Metal ion leaching measured by ICP indicated that while the level of residual Fe ions in solution was too low to detect, that of leached Mn ions was 2.403 mg/L. In the cycle experiments, the catalyst was filtered from the degradation system and dried for use in the next cycle. As shown in Figure 7b, the degradation efficiency showed a small decrease but remained at approximately 74% after four cycles, indicating effective regeneration of FeMn13BTC.

3.3. Catalytic Mechanism

Since porous materials often exhibit a certain degree of pollutant adsorption, OFX adsorption by FeMn13BTC was evaluated. As depicted in Figure 8a, 17.00% of OFX was

removed after 30 min of preadsorption with FeMn13BTC, and then, PAA was introduced to the system to initiate catalytic degradation. Within 2.5 min of PAA addition, 46.97% of OFX was degraded, and the OFX concentration decreased to 36.03% compared to the initial concentration. After reaction for 1 h, the residual OFX was 30.54%. Additionally, the chromatographic peak changed from a single signal before catalysis to multiple signals after catalysis (Figure 8b), indicating the generation of degradation products. The significant decrease in OFX concentration after catalysis as well as the appearance of multiple chromatographic peaks collectively suggested that the main cause of the decrease in OFX concentration was predominantly catalytic degradation based on the FeMn13BTC/PAA system, even though adsorption played a role in OFX removal. The effect of homogeneous catalysis was also investigated. After 30 min of preadsorption, FeMn13BTC was filtered from the solution and PAA was subsequently added, resulting in 37.54% OFX degradation within 1 h (Figure 8a), which indicated that homogeneous catalysis also played a role in OFX degradation.

The reagent for PAA production contained H_2O_2, and the production process also generated H_2O_2. Since H_2O_2 is known to be an oxidant capable of decomposing pollutants,[34] this study sought to exclude potential OFX degradation resulting from H_2O_2. Titration experiments revealed that the mass fraction of H_2O_2 in the prepared PAA solution was 10.91%. As a control group, 5.455 μL of 30% H_2O_2 was used as the
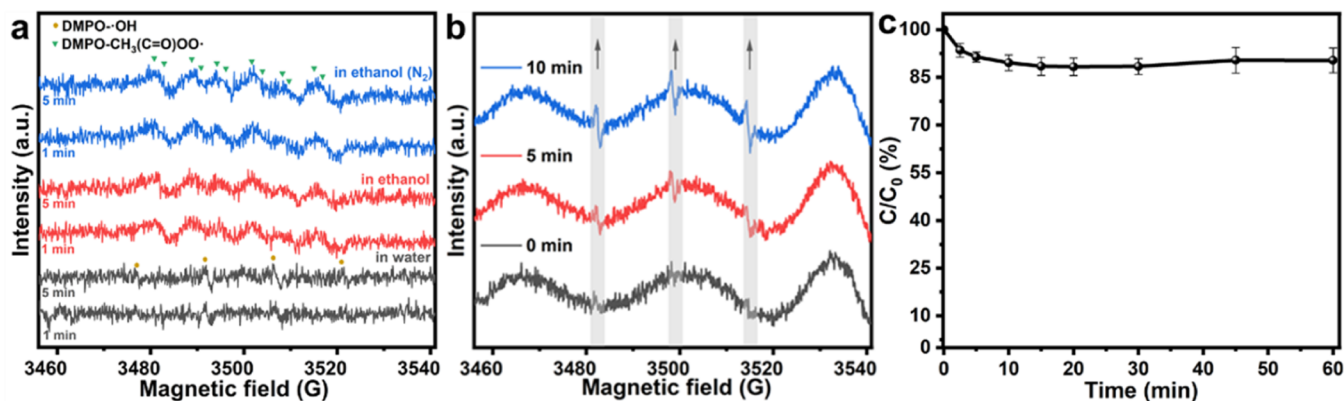
Figure 9. ESR spectra of the FeMn13BTC/PAA system captured by (a) DMPO and (b) TEMP. (c) Carbamazepine degradation in the FeMn13BTC/PAA system. Pollutants 5 mg/L, catalyst 0.1 g/L, PAA 1.034 mM, and pH 7.
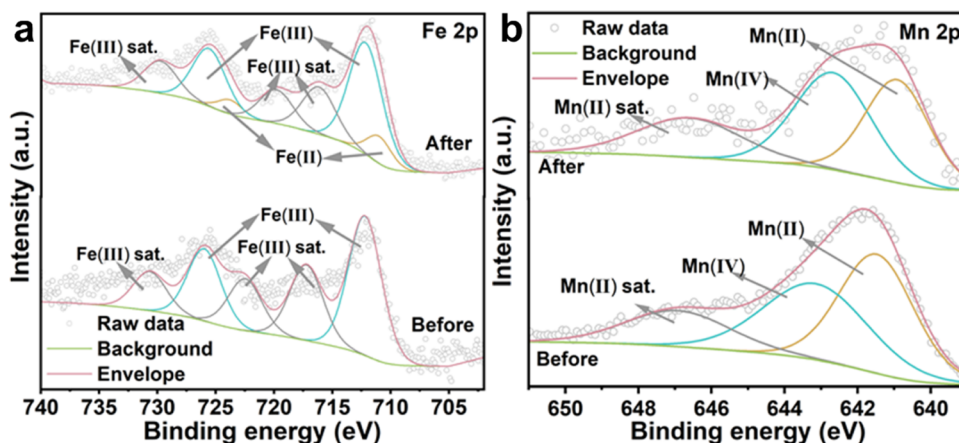

Figure 10. (a) Fe 2p and (b) Mn 2p spectra of FeMn13BTC before and after catalysis.

oxidant instead of PAA. The chromatograms obtained from OFX degradation based on the FeMn13BTC/H_2O_2 system did not exhibit noticeable signal peaks corresponding to degradation products (Figure 8c). These results indicated that H_2O_2 had little effect on OFX degradation in the FeMn13BTC/PAA system, further demonstrating that OFX degradation was primarily attributed to the reactive oxygen species (ROS) generated through the reaction between FeMn13BTC and PAA, instead of the presence of H_2O_2.

To identify the ROS involved in the FeMn13BTC/PAA system, TBA was utilized as a quenching agent for ·OH, while 2,4-hexadiene was used to quench $^\bullet$OH and R−O$^\bullet$.[34,35] However, due to OFX adsorption by FeMn13BTC, quantifying the contributions of $^\bullet$OH and R−O$^\bullet$ was challenging. OFX degradation exhibited only a slight decrease when both quenching agents were employed (Figure S6). To precisely identify the ROS involved, ESR measurements were conducted under different conditions. First, DMPO was used as a trapping agent in the water matrix, with the spectrum displaying a weak $^\bullet$OH peak (Figure 9a). Neither $CH_3C(=O)OO^\bullet$ nor $^\bullet CH_3$ could be observed directly under these conditions.[36,37] The identification of $CH_3C(=O)OO^\bullet$ was completed in an ethanol solution with DMPO (Figure 9a). To exclude any possible influence of $^\bullet OOCH_3$ (which displayed a similar spectrum as $CH_3C(=O)OO^\bullet$ in the system), the measurement was repeated under deprivation of oxygen (nitrogen introduction). The peak intensity of the DMPO adduct did not change considerably after introducing nitrogen,

indicating that $CH_3C(=O)OO^\bullet$ contributed most to the signal (Figure 9a).[36] However, the reaction between $CH_3C(=O)O^\bullet$ and PAA as well as self-decay and self-coupling made $CH_3C(=O)O^\bullet$ difficult to detect.[37] When TEMP was used as a trapping agent, the characteristic three-line spectrum with relative intensities of 1:1:1 confirmed the presence of $^1O_2$[38] (Figure 9b). Nevertheless, the weak signal indicated that $^1O_2$ was not the primary ROS in the FeMn13BTC/PAA system. Carbamazepine (CBZ) is known to react rapidly with $^\bullet$OH and $^1O_2$ while remaining inert to R−O$^\bullet$.[39,40] As depicted in Figure 9c, CBZ degradation in the FeMn13BTC/PAA system was only 9.67%. The above-mentioned results indicated that while $^\bullet$OH and $^1O_2$ contributed to the degradation performance of FeMn13BTC/PAA to some extent, R−O$^\bullet$, especially $CH_3C(=O)OO^\bullet$, played a significant role in the degradation system.

XPS analysis was conducted to study the chemical structure and valence changes of FeMn13BTC before and after the catalytic reaction. The spectra exhibited characteristic peaks corresponding to C, O, Fe, and Mn before and after the reaction (Figure S7). Deconvoluting the Fe 2p spectrum (Figure 10a) revealed that the Fe element existed in the form of Fe(III) before the reaction, according to the double peaks at 712.2 and 726.0 eV, which, respectively, corresponded to the Fe 2p$_{3/2}$ and Fe 2p$_{1/2}$ orbitals. After the catalytic reaction, a new pair of peaks emerged at 710.9 and 723.7 eV, indicating the presence of Fe(II) in the structure.[41] Approximately 9.4% of Fe(III) in the original FeMn13BTC transformed into
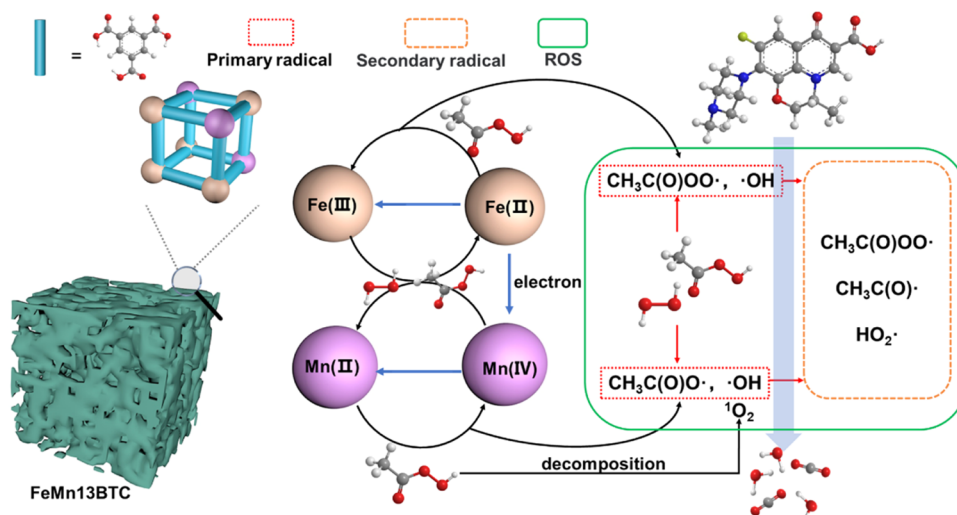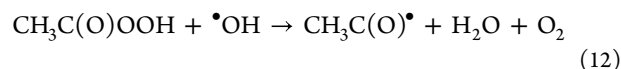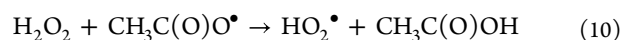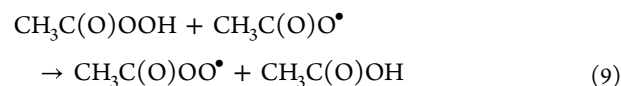
Figure 11. Presumed mechanism of OFX degradation based on FeMn13BTC activating PAA.

Fe(II), giving rise to the coexistence of Fe(II) and Fe(III) in the structure after the catalytic reaction. Furthermore, the proportions of Mn with different valences also changed. Prior to the reaction, the ratio of Mn(II)/Mn(IV) was 52.8:47.2%. However, during the reaction, Mn(IV) gradually became dominant, leading to the ratio decreasing to 47.4:52.6% after the reaction (Figure 10b).

Based on the above-mentioned findings, a reasonable mechanism for OFX degradation based on the FeMn13BTC/PAA system was proposed (Figure 11). W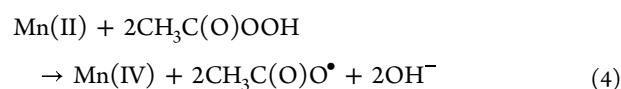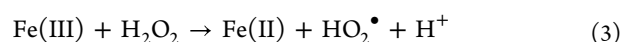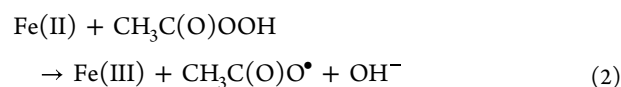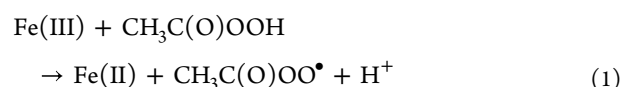hen FeMn13BTC is introduced into the OFX-polluted solution, OFX molecules rapidly diffuse through the catalyst's macropores and mesopores. The catalyst's micropores provide abundant adsorption sites, which allow rapid capture of OFX. Following this step, PAA is introduced into the solution and would quickly spread along the hierarchical porous structure of the catalyst. First, PAA reduces Fe(III) to Fe(II) and produces the primary radical, $CH_3C(O)OO^\bullet$ (eq 1). Then, the generated Fe(II) further reacts with PAA to generate $CH_3C(O)O^\bullet$ (eq 2).[42] Although Fe(III) can react with H_2O_2 existing in the PAA solution, the slow reaction rate suggests that it is not the primary reason for degradation (eq 3).[42] Moreover, PAA oxidizes Mn(II) into Mn(IV) through continuous electron transfer, producing $CH_3C(O)O^\bullet$ (eq 4).[43] Mn(IV) is reduced back to Mn(II) by H_2O_2, forming a redox cycle (eq 5).[44] What is more is that the standard redox potential of Mn(IV)/Mn(II) is higher than that of Fe(III)/Fe(II) (1.23 vs 0.77 V), resulting in electron transfer from Fe(II) to Mn(IV) (eq 6). This electron transfer process generates Mn(II) and Fe(III), which in turn accelerates the redox cycle and formation of primary radicals.[45,46] However, both Fe(II) and Mn(II) may react with PAA to generate $^\bullet OH$, which could be negligible in the process (eqs 7 and 8).[42,43] The generated $CH_3C(O)O^\bullet$ rapidly reacts with PAA and forms more $CH_3C(O)OO^\bullet$, which plays a vital role in OFX degradation (eq 9). Other secondary radicals, most likely contributing minor effects to OFX degradation, are produced by reactions between primary radicals with PAA and H_2O_2 (eqs 10 and 12).[42] According to the literature, $^\bullet CH_3$ could be produced by self-decay of $CH_3C(O)O^\bullet$ (eq 13); however, this trait is not obvious in the process, plausibly because of its low concentration.[37] $^1O_2$ could form via the decomposition of PAA

attacked by peroxy groups, which aligns with the observed increase in the characteristic ESR signal of $^1O_2$ over time (eq 14).[47] In short, with the synergistic effect of Fe and Mn ions, $CH_3C(O)OO^\bullet$ produced by reactions between PAA with metal ions and $CH_3C(O)O^\bullet$ plays a vital role in OFX degradation based on the FeMn13BTC/PAA system. Environmental theoretical calculations could be applied in future analysis to further support the mechanism mentioned above.[48]

$$Fe(III) + CH_3C(O)OOH$$
$$\rightarrow Fe(II) + CH_3C(O)OO^\bullet + H^+ \tag{1}$$

$$Fe(II) + CH_3C(O)OOH$$
$$\rightarrow Fe(III) + CH_3C(O)O^\bullet + OH^- \tag{2}$$

$$Fe(III) + H_2O_2 \rightarrow Fe(II) + HO_2^\bullet + H^+ \tag{3}$$

$$Mn(II) + 2CH_3C(O)OOH$$
$$\rightarrow Mn(IV) + 2CH_3C(O)O^\bullet + 2OH^- \tag{4}$$

$$Mn(IV) + 2H_2O_2 \rightarrow Mn(II) + 2HO_2^\bullet + 2H^+ \tag{5}$$

$$Mn(IV) + 2Fe(II) \rightarrow Mn(II) + 2Fe(III) \tag{6}$$

$$Fe(II) + CH_3C(O)OOH$$
$$\rightarrow Fe(III) + CH_3COO^- + {}^\bullet OH \tag{7}$$

$$Mn(II) + 2CH_3C(O)OOH$$
$$\rightarrow Mn(IV) + 2CH_3COO^- + 2^\bullet OH \tag{8}$$

$$CH_3C(O)OOH + CH_3C(O)O^\bullet$$
$$\rightarrow CH_3C(O)OO^\bullet + CH_3C(O)OH \tag{9}$$

$$H_2O_2 + CH_3C(O)O^\bullet \rightarrow HO_2^\bullet + CH_3C(O)OH \tag{10}$$

$$CH_3C(O)OOH + {}^\bullet OH \rightarrow CH_3C(O)OO^\bullet + H_2O \tag{11}$$

$$CH_3C(O)OOH + {}^\bullet OH \rightarrow CH_3C(O)^\bullet + H_2O + O_2 \tag{12}$$
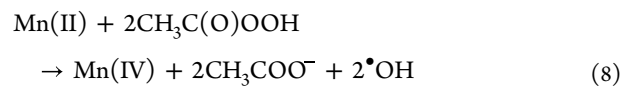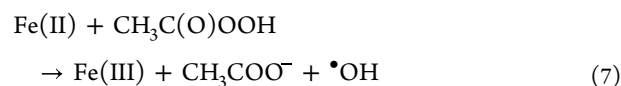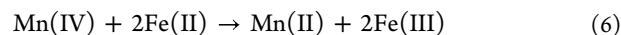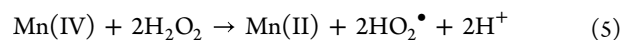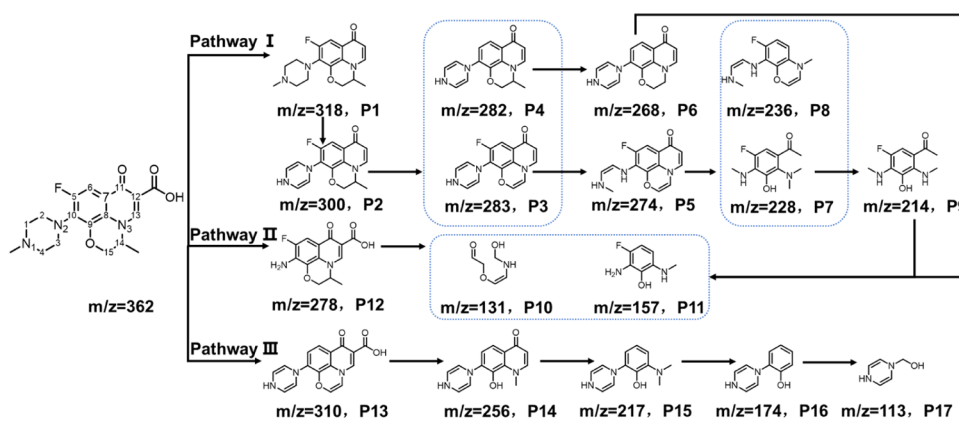
Figure 12. Possible degradation pathways of OFX in the FeMn13BTC/PAA system.

$$CH_3C(O)O^\bullet \rightarrow {}^\bullet CH_3 + CO_2 \tag{13}$$

$$CH_3C(O)OOH + CH_3C(O)OO^-$$
$$\rightarrow CH_3C(O)OH + CH_3C(O)O^- + {}^1O_2 \tag{14}$$
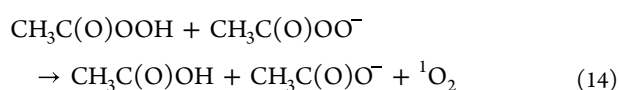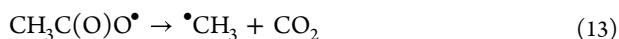
The intermediates formed during OFX degradation by the FeMn13BTC/PAA system were analyzed by using HPLC-QToF-MS (Figure S8 and S9), and three potential degradation pathways were proposed, as shown in Figure 12. In pathway I, degradation is initiated with detachment of the carboxyl group located on the right side of OFX, leading to the formation of product P1 with m/z = 318.[1] P1 undergoes successive attacks from ROS, leading to the loss of a methyl group on the leftmost N atom. The piperazine group undergoes hydroxyl addition followed by elimination reactions, resulting in the formation of the C=C bonds (P2, m/z = 300).[49] P2 can either undergo sequential methyl group detachment, hydroxyl addition, and elimination reactions to form P3 or lose a fluoride group to form P4. ROS attack the double bond in the pyrazine ring of P3, leading to cleavage of the C−N bond and generating P5.[49] P4 undergoes oxidation based on ROS, leading to the detachment of the methyl group at C14 to form P6. The ring-opening reaction of the leftmost aromatic ring in P5 occurs at the double bond, followed by the loss of specific functional groups, leading to the formation of P7 and P8. Further detachment of the methyl group from P7 leads to the formation of P9. In pathway II, degradation is initiated with the cleavage of the piperazine ring, followed by the detachment of the methyl group. ROS attacks lead to oxidation and elimination of the aldehyde group, which in turn lead to the formation of P12 with m/z = 278.[50] The intermediates mentioned above are further oxidized to form P10 and P11. In pathway III, the piperazine and oxygen-containing rings in OFX undergo successive reactions, including detachment of the methyl group, hydroxylation, and formation of the double bond through the elimination reaction, leading to the formation of P13 with m/z = 310.[51] Subsequently, when the carboxyl group is removed from P13, a ring-opening reaction takes place at the C14−C15 position, followed by demethylation, leading to the formation of P14. P15 is then produced through a ring-opening reaction at the C12−C13 position, along with removal of the branch chain containing the carbonyl group. Further elimination of the branch chain at C8 yields P16, which can be epoxidized to form P17.

4. CONCLUSIONS

Herein, the hierarchical micro−meso−macroporous MOG FeMn13BTC was deliberately fabricated to efficiently catalyze PAA activation in order to enhance the antibiotic degradation performance. The MOG synthesis procedure dispensed with supercritical CO_2 and freeze drying, which are typically used to maintain the intact hierarchical porous structure of the MOG during activation, and is thus suitable for future large-scale applications. FeMn13BTC was demonstrated to be an effective catalyst for PAA activation, leading to 81.85% OFX degradation within 1 h. Even in natural water, >80% OFX degradation could be maintained. Cycle experiments proved FeMn13BTC's firm regeneration capability. Characterization analysis and experimental results indicated that Mn ions contributed to the formation of the hierarchical porous structure and facilitated electron transfer between Fe and Mn ions. The two effects collectively produced large amounts of ROS, dominated by R−O$^\bullet$, especially $CH_3C(=O)OO^\bullet$, leading to the superior catalytic performance of FeMn13BTC MOGs compared to the monometallic FeBTC MOG. In conclusion, the study's fabrication strategy for hierarchical porous MOGs through one-pot synthesis and design of a bimetallic catalyst for PAA oxidation should be universally applicable. Moreover, our research sheds light on the fabrication of future hierarchical porous MOF materials and use of the FeMn bimetallic system for PAA-based AOPs as well as PAA-based AOPs for water treatment.

■ ASSOCIATED CONTENT

Ⓢ Supporting Information

The Supporting Information is available free of charge at https://pubs.acs.org/doi/10.1021/acsenvironau.3c00041.

> XRD of the synthesized MOGs; high-resolution TEM and point-of-zero charge of FeMn13BTC; quenching experiment results; total XPS spectra of FeBTC and FeMn13BTC; chromatogram and mass spectra for OFX degradation intermediate determination; and OFX degradation kinetic fitting (PDF)

■ AUTHOR INFORMATION

Corresponding Author

Fengting Li − *State Key Laboratory of Pollution Control and Resources Reuse, College of Environmental Science and Engineering, Tongji University, Shanghai 200092, China; Shanghai Institute of Pollution Control and Ecological*

Security, Shanghai 200092, China; Present
Address: College of Environmental Science &
Engineering, Tongji University, Shanghai 200092, China;
 orcid.org/0000-0003-3467-9827; Phone: +86 21
65987790; Email: fengting@tongji.edu.cn

Authors

Lu Zheng − *State Key Laboratory of Pollution Control and Resources Reuse, College of Environmental Science and Engineering, Tongji University, Shanghai 200092, China; Shanghai Institute of Pollution Control and Ecological Security, Shanghai 200092, China*

Jiarui Fu − *State Key Laboratory of Pollution Control and Resources Reuse, College of Environmental Science and Engineering, Tongji University, Shanghai 200092, China; Shanghai Institute of Pollution Control and Ecological Security, Shanghai 200092, China*

Baolv Hua − *State Key Laboratory of Pollution Control and Resources Reuse, College of Environmental Science and Engineering, Tongji University, Shanghai 200092, China; Shanghai Institute of Pollution Control and Ecological Security, Shanghai 200092, China*

Yi-nan Wu − *State Key Laboratory of Pollution Control and Resources Reuse, College of Environmental Science and Engineering, Tongji University, Shanghai 200092, China; Shanghai Institute of Pollution Control and Ecological Security, Shanghai 200092, China;* orcid.org/0000-0001-6703-019X

Yifan Gu − *State Key Laboratory of Pollution Control and Resources Reuse, College of Environmental Science and Engineering, Tongji University, Shanghai 200092, China; Shanghai Institute of Pollution Control and Ecological Security, Shanghai 200092, China*

Nianqiao Qin − *State Key Laboratory of Pollution Control and Resources Reuse, College of Environmental Science and Engineering, Tongji University, Shanghai 200092, China; Shanghai Institute of Pollution Control and Ecological Security, Shanghai 200092, China*

Complete contact information is available at:
https://pubs.acs.org/10.1021/acsenvironau.3c00041

Author Contributions

CRediT: **Lu Zheng** formal analysis, investigation, project administration, writing-original draft; **Jiarui Fu** conceptualization, writing-review & editing; **Baolv Hua** investigation, writing-review & editing; **Yi-nan Wu** funding acquisition, supervision; **Yifan Gu** funding acquisition, supervision; **Nianqiao Qin** formal analysis, writing-review & editing; **Fengting Li** funding acquisition, supervision.

Notes

The authors declare no competing financial interest.

■ REFERENCES

(1) Li, T.; Lu, S.; Lin, W.; Ren, H.; Zhou, R. Heat-activated persulfate oxidative degradation of ofloxacin: Kinetics, mechanisms, and toxicity assessment. *Chem. Eng. J.* **2022**, *433*, No. 133801.

(2) Lyu, J.; Yang, L.; Zhang, L.; Ye, B.; Wang, L. Antibiotics in soil and water in China—a systematic review and source analysis. *Environ. Pollut.* **2020**, *266*, No. 115147.

(3) Kovalakova, P.; Cizmas, L.; McDonald, T. J.; Marsalek, B.; Feng, M.; Sharma, V. K. Occurrence and toxicity of antibiotics in the aquatic environment: A review. *Chemosphere* **2020**, *251*, No. 126351.

(4) Grenni, P.; Ancona, V.; Caracciolo, A. B. Ecological effects of antibiotics on natural ecosystems: A review. *Microchem. J.* **2018**, *136*, 25−39.

(5) Mahmoodi, N. M.; Keshavarzi, S.; Ghezelbash, M. Synthesis of nanoparticle and modelling of its photocatalytic dye degradation ability from colored wastewater. *J. Environ. Chem. Eng.* **2017**, *5* (4), 3684−3689.

(6) Wang, S.; Wang, H.; Liu, Y.; Fu, Y. Effective degradation of sulfamethoxazole with Fe^{2+}-zeolite/peracetic acid. *Sep. Purif. Technol.* **2020**, *233*, No. 115973.

(7) Zhang, L.; Chen, J.; Zhang, Y.; Xu, Y.; Zheng, T.; Zhou, X. Highly efficient activation of peracetic acid by nano-CuO for carbamazepine degradation in wastewater: The significant role of H_2O_2 and evidence of acetylperoxy radical contribution. *Water Res.* **2022**, *216*, No. 118322.

(8) Ao, X.-w.; Eloranta, J.; Huang, C.-H.; Santoro, D.; Sun, W.-j.; Lu, Z.-d.; Li, C. Peracetic acid-based advanced oxidation processes for decontamination and disinfection of water: A review. *Water Res.* **2021**, *188*, No. 116479.

(9) Correa-Sanchez, S.; Peñuela, G. A. Peracetic acid-based advanced oxidation processes for the degradation of emerging pollutants: A critical review. *J. Water Process Eng.* **2022**, *49*, No. 102986.

(10) Zhang, K.; Zhou, X.; Du, P.; Zhang, T.; Cai, M.; Sun, P.; Huang, C.-H. Oxidation of β-lactam antibiotics by peracetic acid: Reaction kinetics, product and pathway evaluation. *Water Res.* **2017**, *123*, 153−161.

(11) Ao, X.; Zhang, X.; Li, S.; Yang, Y.; Sun, W.; Li, Z. Comprehensive understanding of fluoroquinolone degradation via MPUV/PAA process: Radical chemistry, matrix effects, degradation pathways, and toxicity. *J. Hazard. Mater.* **2023**, *445*, No. 130480.

(12) Ao, X.; Wang, W.; Sun, W.; Lu, Z.; Li, C. Degradation and transformation of norfloxacin in medium-pressure ultraviolet/peracetic acid process: An investigation of the role of pH. *Water Res.* **2021**, *203*, No. 117458.

(13) Qiu, Y.; Zhang, Q.; Wang, Z.; Gao, B.; Fan, Z.; Li, M.; Hao, H.; Wei, X.; Zhong, M. Degradation of anthraquinone dye reactive blue 19 using persulfate activated with Fe/Mn modified biochar: Radical/non-radical mechanisms and fixed-bed reactor study. *Sci. Total Environ.* **2021**, *758*, No. 143584.

(14) Nguyen, T. D.; Phan, N. H.; Do, M. H.; Ngo, K. T. Magnetic Fe_2MO_4 (M:Fe, Mn) activated carbons: Fabrication, characterization and heterogeneous Fenton oxidation of methyl orange. *J. Hazard. Mater.* **2011**, *185* (2), 653−661.

(15) Yan, C.; Jin, J.; Wang, J.; Zhang, F.; Tian, Y.; Liu, C.; Zhang, F.; Cao, L.; Zhou, Y.; Han, Q. Metal-organic frameworks (MOFs) for the efficient removal of contaminants from water: Underlying mechanisms, recent advances, challenges, and future prospects. *Coord. Chem. Rev.* **2022**, *468*, No. 214595.

(16) Bagheri, A.; Hoseinzadeh, H.; Hayati, B.; Mahmoodi, N. M.; Mehraeen, E. Post-synthetic functionalization of the metal-organic framework: Clean synthesis, pollutant removal, and antibacterial activity. *J. Environ. Chem. Eng.* **2021**, *9* (1), No. 104590.

(17) Duan, J.; Chen, L.; Ji, H.; Li, P.; Li, F.; Liu, W. Activation of peracetic acid by metal-organic frameworks (ZIF-67) for efficient degradation of sulfachloropyridazine. *Chin. Chem. Lett.* **2022**, *33* (6), 3172−3176.

(18) Hou, J.; Sapnik, A. F.; Bennett, T. D. Metal-organic framework gels and monoliths. *Chem. Sci.* **2020**, *11* (2), 310−323.

(19) Fu, J.; He, Z.; Schott, E.; Fei, H.; Tu, M.; Wu, Y.-n. Sequential Sol-Gel Self-Assembly and Nonclassical Gel-Crystal Transformation of the Metal-Organic Framework Gel. *Small* **2023**, *19* (18), No. 2206718.

(20) Li, Y.-H.; Wang, C.-C.; Wang, F.; Liu, W.; Chen, L.; Zhao, C.; Fu, H.; Wang, P.; Duan, X. Nearly zero peroxydisulfate consumption for persistent aqueous organic pollutants degradation via nonradical processes supported by in-situ sulfate radical regeneration in defective MIL-88B(Fe). *Appl. Catal., B* **2023**, *331*, No. 122699.

(21) Lohe, M. R.; Rose, M.; Kaskel, S. Metal-organic framework (MOF) aerogels with high micro- and macroporosity. *Chem. Commun.* **2009**, No. 40, 6056−6058.

(22) Mahmood, A.; Xia, W.; Mahmood, N.; Wang, Q.; Zou, R. Hierarchical Heteroaggregation of Binary Metal-Organic Gels with Tunable Porosity and Mixed Valence Metal Sites for Removal of Dyes in Water. *Sci. Rep.* **2015**, *5* (1), No. 10556.

(23) Mahmoodi, N. M.; Abdi, J.; Oveisi, M.; Asli, M. A.; Vossoughi, M. Metal-organic framework (MIL-100 (Fe)): Synthesis, detailed photocatalytic dye degradation ability in colored textile wastewater and recycling. *Mater. Res. Bull.* **2018**, *100*, 357−366.

(24) Jiang, M.; Koizumi, N.; Yamada, M. Adsorption Properties of Iron and Iron-Manganese Catalysts Investigated by in-situ Diffuse Reflectance FTIR Spectroscopy. *J. Phys. Chem. B* **2000**, *104* (32), 7636−7643.

(25) Qian, Q.; Li, Y.; Liu, Y.; Yu, L.; Zhang, G. Ambient Fast Synthesis and Active Sites Deciphering of Hierarchical Foam-Like Trimeta-Organic Framework Nanostructures as a Platform for Highly Efficient Oxygen Evolution Electrocatalysis. *Adv. Mater.* **2019**, *31* (23), No. 1901139.

(26) Torres, N.; Galicia, J.; Plasencia, Y.; Cano, A.; Echevarría, F.; Desdin-Garcia, L. F.; Reguera, E. Implications of structural differences between Cu-BTC and Fe-BTC on their hydrogen storage capacity. *Colloids Surf., A* **2018**, *549*, 138−146.

(27) Zhang, F.; Shi, J.; Jin, Y.; Fu, Y.; Zhong, Y.; Zhu, W. Facile synthesis of MIL-100(Fe) under HF-free conditions and its application in the acetalization of aldehydes with diols. *Chem. Eng. J.* **2015**, *259*, 183−190.

(28) Chen, B.; Yang, X.; Zeng, X.; Huang, Z.; Xiao, J.; Wang, J.; Zhan, G. Multicomponent metal oxides derived from Mn-BTC anchoring with metal acetylacetonate complexes as excellent catalysts for VOCs and CO oxidation. *Chem. Eng. J.* **2020**, *397*, No. 125424.

(29) Cai, G.; Yan, P.; Zhang, L.; Zhou, H.-C.; Jiang, H.-L. Metal-Organic Framework-Based Hierarchically Porous Materials: Synthesis and Applications. *Chem. Rev.* **2021**, *121* (20), 12278−12326.

(30) Huang, G.-X.; Wang, C.-Y.; Yang, C.-W.; Guo, P.-C.; Yu, H.-Q. Degradation of Bisphenol A by Peroxymonosulfate Catalytically Activated with $Mn_{1.8}Fe_{1.2}O_4$ Nanospheres: Synergism between Mn and Fe. *Environ. Sci. Technol.* **2017**, *51* (21), 12611−12618.

(31) Peng, G.; Qi, C.; Wang, X.; Zhou, L.; He, Q.; Zhou, W.; Chen, L. Activation of peroxymonosulfate by calcined electroplating sludge for ofloxacin degradation. *Chemosphere* **2021**, *266*, No. 128944.

(32) Zhang, L.; Chen, J.; Zhang, Y.; Liu, T.; Yao, Q.; Yang, L.; Zhou, X. Interactions between peracetic acid and TiO_2 nanoparticle in wastewater disinfection: Mechanisms and implications. *Chem. Eng. J.* **2021**, *412*, No. 128703.

(33) Wu, Q.; Yang, H.; Kang, L.; Gao, Z.; Ren, F. Fe-based metal-organic frameworks as Fenton-like catalysts for highly efficient degradation of tetracycline hydrochloride over a wide pH range: Acceleration of Fe(II)/ Fe(III) cycle under visible light irradiation. *Appl. Catal., B* **2020**, *263*, No. 118282.

(34) Jiang, Y.; Baimanov, D.; Jin, S.; Law, J. C.-F.; Zhao, P.; Tang, J.; Peng, J.; Wang, L.; Leung, K.S.-Y.; Sheng, W.; Lin, S. In situ turning defects of exfoliated Ti_3C_2 MXene into Fenton-like catalytic active sites. *Proc. Natl. Acad. Sci. U.S.A.* **2023**, *120* (1), No. e2210211120.

(35) Li, R.; Manoli, K.; Kim, J.; Feng, M.; Huang, C.-H.; Sharma, V. K. Peracetic Acid-Ruthenium(III) Oxidation Process for the Degradation of Micropollutants in Water. *Environ. Sci. Technol.* **2021**, *55* (13), 9150−9160.

(36) Chen, L.; Duan, J.; Du, P.; Sun, W.; Lai, B.; Liu, W. Accurate identification of radicals by in-situ electron paramagnetic resonance in ultraviolet-based homogenous advanced oxidation processes. *Water Res.* **2022**, *221*, No. 118747.

(37) Du, P.; Wang, J.; Sun, G.; Chen, L.; Liu, W. Hydrogen atom abstraction mechanism for organic compound oxidation by acetylperoxyl radical in Co(II)/peracetic acid activation system. *Water Res.* **2022**, *212*, No. 118113.

(38) Das, K. C.; Das, C. K. Thioredoxin, a Singlet Oxygen Quencher and Hydroxyl Radical Scavenger: Redox Independent Functions. *Biochem. Biophys. Res. Commun.* **2000**, *277* (2), 443−447.

(39) Wang, J.; Wan, Y.; Ding, J.; Wang, Z.; Ma, J.; Xie, P.; Wiesner, M. R. Thermal Activation of Peracetic Acid in Aquatic Solution: The Mechanism and Application to Degrade Sulfamethoxazole. *Environ. Sci. Technol.* **2020**, *54* (22), 14635−14645.

(40) Liu, B.; Guo, W.; Jia, W.; Wang, H.; Si, Q.; Zhao, Q.; Luo, H.; Jiang, J.; Ren, N. Novel Nonradical Oxidation of Sulfonamide Antibiotics with Co(II)-Doped g-C_3N_4-Activated Peracetic Acid: Role of High-Valent Cobalt-Oxo Species. *Environ. Sci. Technol.* **2021**, *55* (18), 12640−12651.

(41) Yamashita, T.; Hayes, P. Analysis of XPS spectra of Fe^{2+} and Fe^{3+} ions in oxide materials. *Appl. Surf. Sci.* **2008**, *254* (8), 2441−2449.

(42) Kim, J.; Zhang, T.; Liu, W.; Du, P.; Dobson, J. T.; Huang, C.-H. Advanced Oxidation Process with Peracetic Acid and Fe(II) for Contaminant Degradation. *Environ. Sci. Technol.* **2019**, *53* (22), 13312−13322, DOI: 10.1021/acs.est.9b02991.

(43) Kim, J.; Wang, J.; Ashley, D. C.; Sharma, V. K.; Huang, C.-H. Picolinic Acid-Mediated Catalysis of Mn(II) for Peracetic Acid Oxidation Processes: Formation of High-Valent Mn Species *Environ. Sci. Technol.* **2023**, DOI: 10.1021/acs.est.3c00765.

(44) Rothbart, S.; Ember, E. E.; van Eldik, R. Mechanistic studies on the oxidative degradation of Orange II by peracetic acid catalyzed by simple manganese(ii) salts. Tuning the lifetime of the catalyst. *New J. Chem.* **2012**, *36* (3), 732−748.

(45) Liu, Z.; Qin, L.; Lu, B.; Wu, X.; Liang, S.; Zhou, J. Issues and Opportunities Facing Aqueous Mn^{2+}/MnO_2^- based Batteries. *ChemSusChem* **2022**, *15* (10), No. e202200348.

(46) Hou, L.; Li, X.; Yang, Q.; Chen, F.; Wang, S.; Ma, Y.; Wu, Y.; Zhu, X.; Huang, X.; Wang, D. Heterogeneous activation of peroxymonosulfate using Mn-Fe layered double hydroxide: Performance and mechanism for organic pollutant degradation. *Sci. Total Environ.* **2019**, *663*, 453−464.

(47) Wang, Z.; Wang, J.; Xiong, B.; Bai, F.; Wang, S.; Wan, Y.; Zhang, L.; Xie, P.; Wiesner, M. R. Application of Cobalt/Peracetic Acid to Degrade Sulfamethoxazole at Neutral Condition: Efficiency and Mechanisms. *Environ. Sci. Technol.* **2020**, *54* (1), 464−475.

(48) Li, F.; Borthwick, A. G. L.; Liu, W. Environmental theoretical calculation for non-periodic systems. *Trends Chem.* **2023**, *5* (6), 410−414.

(49) Gao, P.; Tian, X.; Nie, Y.; Yang, C.; Zhou, Z.; Wang, Y. Promoted peroxymonosulfate activation into singlet oxygen over perovskite for ofloxacin degradation by controlling the oxygen defect concentration. *Chem. Eng. J.* **2019**, *359*, 828−839.

(50) Li, S.; Wang, C.; Cai, M.; Yang, F.; Liu, Y.; Chen, J.; Zhang, P.; Li, X.; Chen, X. Facile fabrication of TaON/Bi_2MoO_6 core-shell S-scheme heterojunction nanofibers for boosting visible-light catalytic levofloxacin degradation and Cr(VI) reduction. *Chem. Eng. J.* **2022**, *428*, No. 131158.

(51) Liu, G.; Zhang, Y.; Yu, H.; Jin, R.; Zhou, J. Acceleration of goethite-catalyzed Fenton-like oxidation of ofloxacin by biochar. *J. Hazard. Mater.* **2020**, *397*, No. 122783.